Results in Engineering 15 (2022) 100462

Contents lists available at ScienceDirect

Results in Engineering

journal homepage: www.sciencedirect.com/journal/results-in-engineering

Numerical study of effects of solid particle erosion on compressor and engine performance

Jasem Alqallaf [a,b,*], Joao A. Teixeira [a]

[a] School of Aerospace, Transport and Manufacturing, Cranfield University, Cranfield, Bedford, MK43 0AL, UK
[b] Kuwait Army, Kuwait Ministry of Defense, Safat, 13128, Kuwait

ARTICLE INFO

Keywords:
Blade surface
Computational fluid dynamics
Compressor
Cycle performance
Efficiency
Solid particle erosion

ABSTRACT

Solid particle erosion (SPE) is a major source of damage to, and cause of failure of, turbomachinery, including centrifugal and axial compressors and gas turbines. There is considerable interest within the turbomachinery industry to develop the means to enhance durability and improve prediction of likely breakdowns of machinery operating in locations and conditions where ingestion of, for example, dust and sand grains is unavoidable during operation. The present study examines the implications of degradation of the compressor on gas turbine cycle performance, caused by operating in eroding environments, linking compressor aerodynamics with the thermodynamic cycle. The research engine employed in the study comprised a fan, bypass, and two stages of the low-pressure compressor (booster). A numerical simulation using Computational Fluid Dynamics (CFD) software was performed to predict the likely erosion patterns due to solid particles (SPs) impacting on the blades of the first two stages of an axial compressor. This study introduces a method that provides the freedom to apply roughness to a particular region of the blade following the SPE patterns identified as part of the CFD simulations so as to represent the effects of the erosion spots on the overall flow field. The localised roughness method employs a perturbation of the geometry of the blade in the regions corresponding to the location predicted by the SPE model. The intensity of the perturbation, which is governed by a "fraction factor" coded in a Matlab script, was calibrated by reference to a roughness case, applied over the entire blade surface, with equivalent sand-grain roughness (k_s) of 60 μm. Turbomatch, the Cranfield in-house gas turbine performance simulation software, was employed to model the degradation of engine performance. The research confirmed that SPE is linked with significant decreases in engine performance parameters such as isentropic efficiency (η_{is}) and pressure ratio (PR). These quantities showed, for the SPE cases considered, a drop of 8.8% and 5.2%, respectively. These findings are useful to link local SPE events to global GTE cycle performance.

1. Introduction

Aviation engineers deal daily with many different threats posed to aircraft, especially, to gas turbine engines (GTEs) due to environmental hazards. Such hazards can result in operational disruption such as scheduling problems, flight delays and cancellations and, occasionally, threats to the safety of passengers and/or crew [1]. Aero-engines often operate in inhospitable environments whereby significant amounts of particulates of different sizes are ingested by the GTEs. This can lead to significant degradation of the structure of GTE components and a deterioration of the engine performance [2,3]. In particular, the performance of GTEs is dependent on the efficiency of the compressor, and so it is necessary to ensure the compressor always works under optimum conditions [4]. One cause of deterioration in the performance of a compressor is solid particle erosion (SPE), due to ingestion of sand or biological matter [5]. This is an extensive problem because in the real-world GTEs often operate in dusty atmospheres which means that the compressor blades are continuously bombarded with dust particles of various types. The degree and extent of the wear will depend on numerous factors but especially the velocity of the impacting solid particles and the angle at which they impact the GTE component [6].

The main causes of SPE can be listed as: (1) sand carried to high altitudes by sandstorms; (2) particles of dirt, sand, etc., carried from the ground to the engine intake by vortices created whilst the engine operates in a high power setting; (3) thrust reversal used to reduce landing distance which occurs at relatively low speeds and can blow dirt, sand and other debris into the engine [2]. Such processes are clearly

* Corresponding author. School of Aerospace, Transport and Manufacturing, Cranfield University, Cranfield, Bedford MK43 0AL, UK.,
E-mail addresses: j.alqallaf@cranfield.ac.uk (J. Alqallaf), j.a.amaral.teixeira@cranfield.ac.uk (J.A. Teixeira).

https://doi.org/10.1016/j.rineng.2022.100462
Received 24 January 2022; Received in revised form 25 March 2022; Accepted 22 May 2022
Available online 11 June 2022
2590-1230/© 2022 The Author(s). Published by Elsevier B.V. This is an open access article under the CC BY license (http://creativecommons.org/licenses/by/4.0/).

Nomenclature

CFD	Computational fluid dynamics
C_D	Drag coefficient
C_{LS}	Lift coefficient
DP	Design point
d_P	Solid particle diameter (m)
E	Erosion rate
EGV	Exit guide vanes
EPR	Engine pressure ratio
E3	Energy Efficient Engine
F_D	Drag force acting per unit particle mass (N)
F_G	Gravitational force per unit mass (m/s^2)
F_P	Force per unit mass (N/kg)
F_S	Saffman force
F_V	Virtual mass force
g	Gravitational force per unit mass
GTE	Gas turbine engine
HPC	High pressure compressor
HPT	High pressure turbine
IGV	Inlet guide vanes
k_s	Equivalent sand-grain roughness (μm)
k_1, k_2, k_3, k_4, k_{12}	Dimensionless constants
LE	Leading edge of the blade
LPC	Low pressure compressor
LPT	Low pressure turbine
$\dot{m}$	Mass flow rate (kg/s)
m_p	Particle mass (kg)
$\dot{N}$	Number of impact particles
NDMF	Non-dimensional mass flow
PS	Pressure side
P_s	Static pressure (Pa)
PR	Pressure ratio
P_{01}	Total pressure (Pa)
RANS	Reynolds Averaged Navier-Stokes
R_{ek}	Reynolds number
R_{eS}	Shear flow Reynolds number
R_{ep}	Particle Reynolds number
SFC	Specific fuel consumption (g/kN.s)
SiO_2	Silicon dioxide
SPE	Solid particle erosion
SPs	Solid particles
SS	Suction side
SST	Shear stress transport turbulence model
TE	Trailing edge of the blade
TET	Turbine entry temperature (K)
T_{01}	Total temperature (K)
V_P	Particle velocity (m/s)
V_f	Fluid flow velocity (m/s)
V_1, V_2, V_3	Reference velocities (m/s)

Greek letters

ρ_f	Fluid density (kg/m^3)
ρ_p	Particle density (g/cm^2)
μ_f	Fluid viscosity (N s m^{-2})
γ	Impact angle (Deg)
γ_0	Impact angle of maximum erosion (Deg)
Ω_f	Rotational speed of sphere (rad/s)
η_{is}	Isentropic efficiency

dynamic in character and when solid particles (SPs) strike the turbine blades even small particles can cause significant damage [7]. This type of damage is most common in the compression system of the GTE, including the fan and the low-pressure compressor (LPC). The LPC blades can be eroded, leading to a gradual decline in aerodynamic performance and structural integrity [8]. The increase in roughness entails a drop of the mass flow of the engine due to added blockage and this is accompanied by falls in pressure ratio and efficiency. There have been reports in the literature of losses in efficiency and power output ranging from 2% for mild roughness to 15–20% for heavily roughened blade surfaces [9,10]. Hence, continuous operation where particles are entering the engine inlet will diminish engine performance, reduce the working lives of components and affect their reliability [11].

Hamed et al. [12], presented a review of published work relating to the deterioration of turbomachines and found ample evidence of the link between blade surface condition and degradation of engine performance. The authors listed a number of modifications of the blade geometry of compressors brought about by erosion namely, blade chord reduction, increase in tip clearance, added surface roughness and increase in leading and trailing edge sharpness all of which caused degradation of cycle performance.

Ghenaiet [13], investigated numerically the dynamics of SPE in the initial turbofan stage of a GTE where the incoming air undergoes low pressure compression. The software used simulated the trajectories of the particles by solving, in a stepwise manner, their equations of motion. The diameters of the particles (assumed to be sand) were in a theoretical range of 0–1000 μm and the concentrations were in the range 50–70 mg/m^3. The author claimed that both ranges corresponded to known sand particle distributions. The simulations predicted that the major areas of erosion would be located along the leading edge (LE) and near to the hub and shroud of the blades forming the inlet guide vanes (IGV). In addition the rotor blades would suffer significant erosion of the LE and the trailing edge (TE) with distortion of the blade tips. Lastly the diffuser erosion was likely to be observed not only on the LEs and TEs but also over the surfaces of the blades.

Suzuki and Yamamoto [14], used a computational fluid dynamics (CFD) software to investigate the SPE phenomena in a two stage compressor with a fixed wheel speed of 5000 rpm and mass flow rate of 1.73 kg/s. The particle diameters for the two cases studied were set as 5 and 165 μm. The researchers concluded that (1) the regions most affected were the LE and the pressure side (PS) of the rotor blade; (2) the SPs were transported in the direction of the blade tip by the centrifugal forces; (3) the velocities of the SPs at the second stage were lower than the first stage due to particle-wall impact; (4) the regions of erosion on the LE and the tip of the second stage blades were smaller than for the first stage.

Poursaeidi et al. [15], performed a numerical and experimental examination of SPE effects on the blades of the first stage of an axial compressor using stainless steel as the material of the blades and an erosion test bench. CFD software was used for the numerical analysis. The mass flow rate and particle diameters were set to 144 kg/s and 40 μm, respectively. The research outcomes show that the least erosion took place on the IGV blades, with the maximum erosion rate occurring at the tip of the rotor blade and on the hub of the stator blade near to the LE.

Tabakoff [16], used an erosion tunnel to investigate how SPE affected the deterioration of performance of a single-stage axial flow compressor. The design specifications of the compressor were: mass flow rate 3.67 kg/s, rotational speed 9000 rpm, tip diameter 300 mm, pressure ratio 1.1, hub-to-tip ratio 0.75. Blade erosion was examined in five stages, with 5 kg of sand used in each stage over an interval of 121 s. The study results demonstrated that: (1) erosion was found on both sides of the blades near the LE, (2) the blade chord decreased by 1.2%, (3) the tip clearance of the rotor increased by 300 μm, (4) the increase in surface roughness on the PS was in the range 20–70 μm. The performance of the

tested compressor showed deteriorations in stage loading of 2.4%, 3.32% and 4.27% at mass flows of 1.36 kg/s, 1.732 kg/s, and 2.00 kg/s, respectively.

The current research employed a low-pressure compressor model, designed in-house and inspired by NASA's Energy Efficient Engine (E3) engine [17–19]. The compressor model was assembled by a preceding research team at Cranfield University to investigate GTE deterioration recovery techniques. The present research investigates the performance degradation due to the action of SPE on the first two stages of the LPC. The work employed the commercial CFD code ANSYS CFX 19.1 to simulate numerically the flow field within the LPC. Those analyses were complemented by thermodynamic investigations of the GTE carried out with the Turbomatch 0-D performance simulation software developed in-house at Cranfield University. This approach enabled us to link the aerodynamic, SPE, blade roughness and GTE cycle deterioration effects and by doing so to understand the interdependency of the various parameters involved. Thus, the present work contains an element of novelty, in terms of the available literature, through the connection of the detailed LPC aerodynamic analyses with the means of evaluation of the GTE cycle performance implications, which are due to SPE action.

2. Modelling of solid particle erosion

SPE increases the roughness of blade surfaces, weakens the structure of compressor blades, and increases cycle losses [20]. Industrially important, SPE has been investigated many times with a multitude of papers available in the literature, some of which were experimental investigations while others developed models for numerical simulation. The latter were often based on theoretical studies which proposed new mechanisms and scenarios to describe SPE [5,21]. In this research, CFD-based erosion modelling will be demonstrated in detail, investigating three major stages for predicting SPE damage for a given geometry and flow conditions: (1) flow field modelling; (2) particle trajectory and (3) erosion prediction using equations that can mathematically model and approximately predict erosion rates [22]. Such a process, if effective would enhance design methodology for GTEs operating in arid environments whilst guiding the erosion protection of its turbomachinery elements. Nevertheless, since each step in the process depends on the previous one, any inaccuracies in the earlier steps will affect the final erosion prediction results [21,23].

2.1. Flow field modelling

Flow field modelling is the basis of SPE predictions when using CFD. Simulations of the trajectories of SPs as they pass through the turbomachinery are obtained by solving both the equations of motion of the SPs (usually by numerical integration), and the three dimensional Reynolds Averaged Navier-Stokes (RANS) equations for turbulent flow [24]. The CFX software, can simulate multiphase flows via a model selected as most appropriate for the secondary phase; bubble, droplet, or solid particle (SP). Generally, either the Eulerian-Eulerian multiphase model or Eulerian-Lagrangian particle tracking model is used. The former considers both phases to exist simultaneously, so their motion is considered as homogeneous and particle movement is due to a concentration gradient. Here the velocity of the SP is averaged over each cell of the mesh being used. This approach can be computationally expensive as the required computing power is proportional to the number of classes of particles, and the equations must be solved for each class (size) of particle for each time step [23]. The Eulerian-Eulerian approach is problematic when simulating the behaviour of particles close to a solid boundary where the motion of the particles may include impacts and rebounds. However, the Eulerian-Eulerian approach will give only the mean value for the motion of a specific particle in a control volume. This is important when considering solid particle impacts and the resulting erosion because it inaccurately predicts the impact velocity and this will affect the predicted erosion [25]. Eulerian-Lagrangian models for a continuous phase utilise a Eulerian reference frame, and then the dispersed solid particles will be modelled independently utilising Lagrangian tracking algorithms [23,26].

2.2. Particle trajectory

Generally, Eulerian-Lagrangian models associated with one-way coupling between particles and flow are used to simulate the trajectory of particles. Utilisation of the coupling method in multiphase particle models introduces the degree of transferred forces between those phases, where: (1) One-way coupling - the forces are transmitted to the particles by the continuous phase without any back forces being transferred by the particles to the continuous phase, (2) Two-way coupling - both continuous phase and the particles transmit forces to one another, and (3) Four-way coupling - much the same as two-way coupling, but forces can also be transferred between particles. As the continuous phase can be considered unaltered by the presence of small-size particles, one-way coupling is deemed appropriate for this study. With this assumption the particles do not transfer forces back to the continuous phase (due to their negligible momentum) which significantly reduces the computational cost [27,28]. The Lagrangian method allows consideration of different starting points when tracking single particles, which allows more flexibility to manage in greater detail certain important physical features, in particular wall-particle interactions. This method neglects the effects of the particle phase on the solutions of the flow field because the particles comprise an insignificant volume fraction, which reduces the computational cost [29]. Equation (1) shows the most commonly used equation of motion for solid particles as used in CFD [21,24,30–32]:

$$\frac{dV_P}{dt} = F_V + F_P + F_G + F_D \tag{1}$$

Where V_P is the particle velocity, F_V virtual mass force, F_P is the force per unit mass that exists due to the pressure gradient, F_G is the gravitational force per unit mass and F_D is the drag force acting per unit particle mass.

The virtual mass (F_V) is a force that acts when a volume of fluid is displaced by a particle within the fluid accelerating relative to the fluid. F_V can be represented as follows:

$$F_V = \frac{1}{2}\frac{\rho_f}{\rho_p}\frac{d}{dt}\left(V_f - V_P\right) \tag{2}$$

Where ρ_f is the fluid density, ρ_p is the particle density, V_f is the fluid flow velocity and V_P is the particle velocity.

The pressure gradient (F_P) will have a major impact on the trajectory of the particle if the particle passes through a region with high pressure gradient. F_P is represented as:

$$F_P = \left(\frac{\rho_f}{\rho_p}\right) V_{Pi}\frac{d\,V_f}{d\,x_i} \tag{3}$$

Gravity and buoyancy forces can affect a particle's trajectory:

$$F_G = \frac{\left(\rho_p - \rho_f\right) g}{\rho_p} \tag{4}$$

Drag force (F_D) is the greatest force acting per unit mass of the particle. The effects of the viscous and inertial regimes in the transition region, for spherical particles ($0.1 < R_e < 1000$), are significant. Thus, the dimensionless drag coefficient (C_D) is a complicated function of Reynolds number (R_e) and required to be investigated experimentally. Different empirical correlations associated with experimental data have been examined. However, in CFX, only the Schiller and Naumann correlation is implemented. F_D can be represented in terms of the C_D as follows [31]:

$$C_D = \frac{24}{Re_p}\left(1 + 0.15 Re_P^{0.687}\right) \tag{5}$$

In addition, CFX enhanced the Schiller and Naumann empirical correlation to ensure the accurate limiting behaviour of the inertial regime as follows:

$$C_D = \max\left(\frac{24}{Re_p}\left(1 + 0.15 Re_P^{0.687}\right),\ 0.44\right) \tag{6}$$

$$R_{ep} = \frac{\rho_f}{\mu_f} d_p \left| V_f - V_P \right| \tag{7}$$

Where d_P is the particle diameter, ρ_f is fluid density, ρ_p is density of particle, μ_f is the fluid viscosity, C_D is the drag coefficient, R_{ep} is the particle Reynolds number, V_f is the fluid flow velocity, V_P is the particle velocity and g is the gravitational force per unit mass.

For Re_p that are large enough for inertial effects to dominate over the viscous effects, the C_D becomes independent of Re_p and the C_D can be calculated from the expression below [31]:

$$C_D = 0.44, 1000 \le Re_p \le 1 - 2\text{x}10^5 \tag{8}$$

When the particle size is sufficiently large, and simultaneously the velocity gradient is large, a significant lift force at right angles to the flow will be exerted on the particle due to a shearing force exerted by the fluid, known as the Saffman force (F_S) [24]:

$$F_S = \frac{\pi \rho_f}{8} d_p^3 C_{LS} \left(V_f - V_P\right) . \nabla V_f \tag{9}$$

Where:

$$C_{LS} = \frac{4.1126}{\sqrt{\text{Re}_S}} f\left(\text{R}_{ep},\ \text{R}_{eS}\right) \tag{10}$$

$$\text{R}_{eS} = \frac{\rho_f}{\mu_f} d_p^2 \left| \Omega_f \right| \tag{11}$$

Where the symbols are as defined above with the addition that, C_{LS} is the lift coefficient, Re_S is the shear flow Reynolds number, and Ω_f is the rotational speed of a sphere.

2.3. Erosion modelling

The erosion models depend on the physical properties of both base surface material and the particle, including particle diameter, concentration, velocity and impact angle, and specimen width [33]. To date, of the many models for evaluating SPE proposed in the literature only two are supported in the CFX software [34]. One is Finnie's model [35] where erosion is determined by the angle of impact and particle speed. However, the rebound erosion model developed by Tabakoff and Grant [36] has been found to be more accurate than Finnie's given that it employs a formulation utilising a greater number of parameters [34,37,38]. Thus, the Tabakoff and Grant model was used in this study.

In the Tabakoff and Grant erosion model, the erosion rate is represented as [31]:

$$E = f(\gamma)\left(\frac{V_P}{V_1}\right)^2 cos^2\,\gamma\left[1 - R_T^2\right] + f(V_{PN}) \tag{12}$$

where:

$$f(\gamma) = \left[1 + k_2\, k_{12} \sin\left(\gamma \frac{\frac{\pi}{2}}{\gamma_0}\right)\right]^2 \tag{13}$$

$$R_T = 1 - \frac{V_P}{V_3}\sin\gamma \tag{14}$$

$$f(V_{PN}) = \left(\frac{V_P}{V_2}\sin\gamma\right)^4 \tag{15}$$

$$k_2 = \left\{ \begin{array}{l} 1.0\ if\ \gamma \le 2\,\gamma_0 \\ 0.0\ if\ \gamma > 2\,\gamma_0 \end{array} \right\} \tag{16}$$

where E is the erosion rate (a dimensionless mass: mass of eroded wall material divided by the mass of particle), V_P is the particle velocity, k_2 and k_{12} are dimensionless constants, γ is the impact angle, and γ_0 is the impact angle of maximum erosion.

The constants contained in the Tabakoff and Grant erosion model equations have the dimension of velocity to make the model function for more general erosion cases. Table 1 lists the constants that link the original model and CFX software.Where:

$$V_1 = 1\Big/\sqrt{k_1} \tag{17}$$

$$V_2 = 1\Big/\sqrt{4k_3} \tag{18}$$

$$V_3 = 1/k_4 \tag{19}$$

Where, k_1, k_3 and k_4 are dimensionless constants.

The overall erosion rate and erosion output due to SPE can be calculated from the following expression [31]:

$$Overall\ erosion\ rate = E\,\dot{N}\,m_p \tag{20}$$

Where, E is the erosion rate, $\dot{N}$ is the number of particles impacts per unit time, and m_p is the mass of the particle.

In the front sections of gas turbine engines, given that the air temperature is initially low, the components used in these sectors tend to be made of aluminium or titanium (Ti) alloys with superalloys being selected as temperatures exceed approximately 400 °C [39]. The Tabakoff and Grant erosion model employs a combination of materials to characterise the interaction between the abrading airborne particles (eg silica sand) which strike an abradable target surface (eg 2024 aluminium alloy). The Tabakoff erosion model constants and functions were determined experimentally.

Of the available material combinations implemented in CFX the quartz-aluminium one was selected for this study as shown in Table 2. Although aluminium can be found in GTEs low pressure compression systems, Ti based alloys are in widespread use, and their employment within an erosion model would represent an expansion of the generality and representativeness of the present study. That however would require the performing of experiments which were not within the scope of the current research project.

3. Computational approach

The computed cases were examined using steady state Reynolds Averaged Navier Stokes (RANS) simulations together with the k-ω shear stress transport (SST) turbulence model. The simulations were performed in Cranfield's Delta High-Performance Computer cluster (HPC-Delta) employing 32 CPUs.

Table 1
Constants in Tabakoff and Grant erosion model as used in the CFX software [31].

Value	Dimensions	CFX-Pre Variables
k_{12}	Dimensionless	Constant
k_2	Dimensionless	Constant
V_1	Velocity	Reference velocity 1
V_2	Velocity	Reference velocity 2
V_3	Velocity	Reference velocity 3
γ_0	Degrees	Angle of maximum erosion

Table 2
Coefficients of quartz-aluminium used in the Tabakoff erosion model [23].

Variable	Coefficient	Value
k_{12}	k_{12}	5.85 x 10^{-1}
Reference velocity 1	V_1	159.11 [m/s]
Reference velocity 2	V_2	194.75 [m/s]
Reference velocity 3	V_3	190.5 [m/s]
Angle of maximum erosion	γ_0	25 [degrees]

3.1. Model description

As stated above the aero-engine model used was developed by a Cranfield University research team based on the NASA's Energy Efficient *Engine* (E3) [17–19]. The components of the research engine used in this investigation include the fan (R1), bypass ducting (EGV) and the first two stages of the LPC, Fig. 1.

The design parameters of the research engine at design point (DP) are shown in Table 3.

3.2. Mesh generation

The Turbogrid meshing tool, which is part of the ANSYS CFX suite, was employed to generate structured meshes. Fig. 2 presents a surface mesh of the hub region together with details of the mesh at the midspan LE and TE of the blade. Information regarding the model verification which involved the assessment of the dependency of the results on the mesh size can be found in Ref. [40]. The mesh employed in the current study corresponds to the fine mesh used in mesh dependency analysis. The number of nodes of the simulated components is 1.1 million nodes for the bypass, IGV, R2, S2, R3 and S3 components, and 1.6 million nodes for the fan components.

3.3. Boundary conditions and convergence criteria

Fig. 3 shows a sketch of the dimensions of the computational domain expressed in terms of the midspan fan blade chord together with the location of the main boundary conditions (BC).

A single periodic passage of each LPC blade row was simulated at the DP. Mixing planes were used as the interface between stator and rotor rows. All cases converged with residual values of mass less than 10^{-5}, and residual values of momentum less than 10^{-4}. The boundary conditions are described as follows, Table 4.

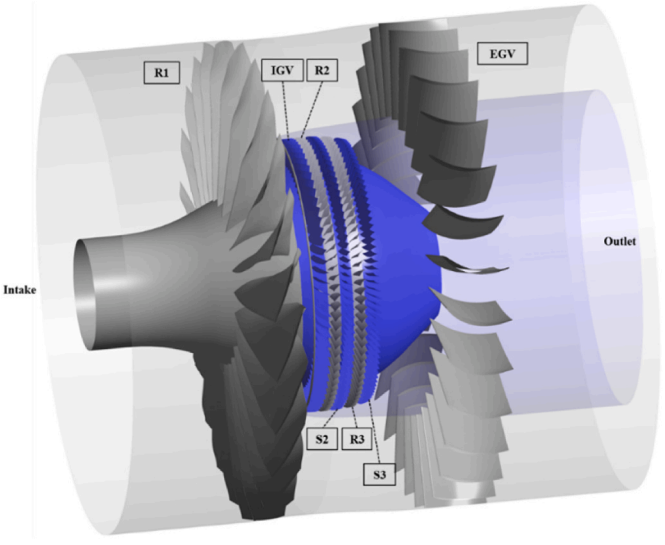


Fig. 1. Computational domains and blading of the fan, EGV and booster IGV and first two stages.

Table 3
Fan, bypass, and low pressure compressor (LPC) design parameters. Reprinted with permission from Refs. [17–19]. Copyright 2013 NASA Technical Report Server (NTRS).

Items	Unit	Value
Fan pressure ratio	–	1.74
Number of fan blades (R1)	–	24
R1 tip clearance	mm	1.39
Number of exit guide vanes (EGV) blades	–	29
Number of inlet guide vanes (IGV) blades	–	76
Number of second rotor blades (R2)	–	82
R2 tip clearance	mm	0.97
Number of stator blades (S2)	–	102
Number of third rotor blades (R3)	–	88
R3 tip clearance	mm	0.86
Number of third stator blades (S3)	–	110
Total mass flow rate ($\dot{m}$) (100% speed-line)	kg/s	623.72
$\dot{m}$ (EGV) (100% speed-line)	kg/s	540.67
$\dot{m}$ (LPC) (100% speed-line)	kg/s	83.05
PR (LPC) (for the four stages)	–	1.77
PR (LPC) (for the first two stages)	–	1.33
Rotational speed for 100% speed-line	rpm	4215

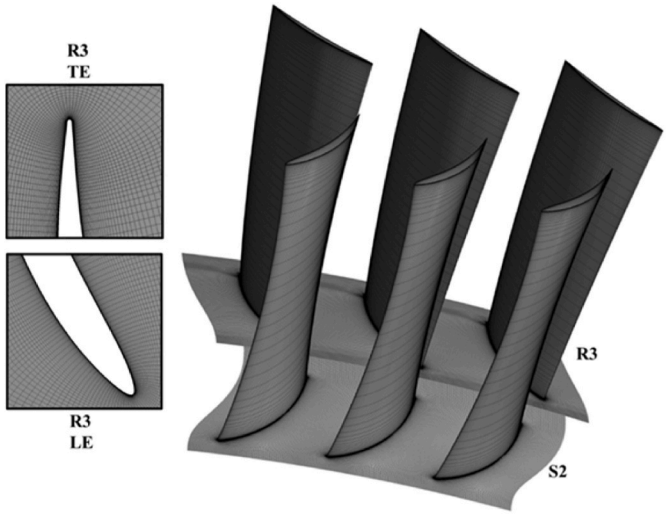


Fig. 2. S2 and R3 grids, and details of R3 LE and TE.

3.4. Simulations setup for solid particle erosion studies

This section describes the numerical setup employed for SPE modelling of the research engine. Details of the SPE model setup are as follows:

3.4.1. Particle definition

For the current study, the solid particles are specified as silicon dioxide (SiO_2) given that SiO_2 is the major constituent of sand [41]. Small-scale particles will follow the fluid flow path more strictly than larger diameter particles and tend to hit the target surface over a broader area, with few particle–particle interactions. Similarly, the likelihood of more than one particle impacting the same spot is low [42,43]. According to Loud and Slaterpryce [44], solid particles with diameters of 20 μm and above (when present in sufficient quantities) can lead to SPE of compressors blades. Thus, the particle diameter distribution was set to the range of minimum diameter 20 μm and maximum diameter 80 μm, with a normal distribution. The normal distribution requires the prescription of minimum and maximum diameters, mean diameter and standard deviation in diameter. The particle shape factor was neglected in the current study.

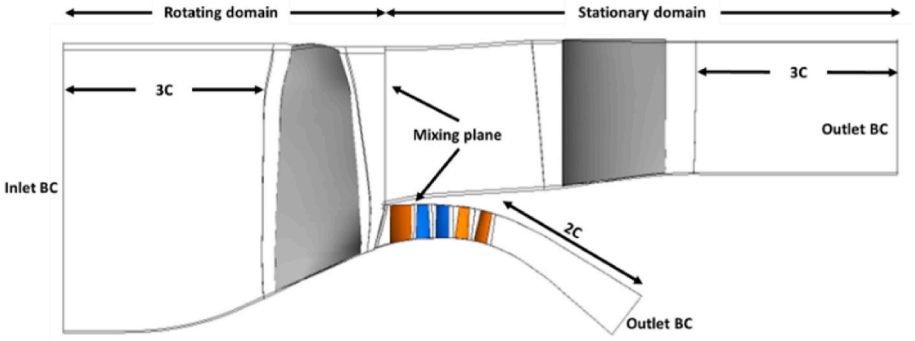


Fig. 3. Computational domain and boundary conditions location.

Table 4
Research engine boundary conditions.

Boundary condition	Type	Value
Fan inlet (stationary frame)	total pressure (P_{01}) & temperature (T_{01})	P_{01} = 101.325 KPa T_{01} = 288.15 K
Fan, R2 and R3 domains	Rotating domain	4215 rpm
EGV, IGV, S2 and S3	Stationary domain	–
Walls	Non slip	–
EGV outlet	Average static pressure (P_s)	147.338 kPa
S3 outlet	Average static pressure (P_s)	159.504 kPa

3.4.2. Particle injection

The SPs injected into the fan (R1) inlet divided between those flowing into the bypass and those flowing into the LPC of the research engine. The zero-slip velocity option in CFX causes the particles to be injected at the local velocity of the continuous phase [31]. It can be used as an inflow boundary when specifying either mass flow or total pressure for the continuous phase. Uniform injection was assumed so that the SPs were injected with even spatial distribution and at equal time intervals into the inlet domain of the research engine.

3.4.3. Solver settings

As the one-way phase coupling approach was employed in this study, the particle tracking information could be obtained after running a single iteration following from a clean field simulation in order to decrease the computational cost. The ANSYS CFX software computed the particle trajectories of the one-way coupled approach once the continuous phase met its residual targets. The time required to process the simulated solid particle trajectories in the HPC-Delta system was about 40 min. Further discussion and description of particle ingestion and trajectories modelling within ANSYS CFX can be found in Refs. [23, 31]. The summary of the simulation setup, utilising the CFX-Pre tool, for the SPE study is shown in Table 5.

3.5. Computational fluid dynamics results comparison

The CFD and Turbomatch findings were compared versus the NASA E3 data presented in Refs. [17–19]. The results of the pressure ratio (PR) against the non-dimensional mass flow (NDMF) for the 100% speed-line of the fan are presented in Fig. 4. As can be seen the agreement between the computed values and the reported design quantities is very close.

An equivalent evaluation between numerical predications and the reported design values applicable to the first two stages of the booster is presented next, Table 6. The results present a reasonably good agreement with the difference between the CFD findings and the engine design calculations being below 4%.

In this study, three different scenarios (cases) were simulated regarding the blade surfaces of the LPC as follows:

Table 5
The setup outlines of SPE study.

Variable	Value	Unit
Fluid definition		
Air (ideal gas)	–	–
Morphology	Continuous fluid	–
Heat transfer	Isothermal	–
Fluid temperature	300	K
Particle definition		
Thermodynamic state	Solid	–
Molar mass	60.08	[g mol^{-1}]
Density	2270	[kg m^{-3}]
Specific heat capacity	0	[J kg^{-1} K^{-1}]
Morphology	Particle transport solid	Eulerian-Lagrangian
Particle diameter distribution	Normal in diameter by mass	–
Minimum diameter	20×10^{-06}	m
Maximum diameter	80×10^{-06}	m
Mean diameter	50×10^{-06}	m
Standard deviation	42.42×10^{-06}	m
Erosion model	Tabakoff and Grant (Coefficients of quartz-aluminium material)	–
Heat transfer model	None	–
Rough wall model	None	–
Fluid/particle definition		
Particle coupling	One-way coupling	–
Drag force	Schiller Naumann	–
Inlet of fan (R1)		
Mass and momentum	Zero slip velocity	–
Particle position	Uniform injection	–
Number of positions	Direct specification	–
Number of particles	200,000	–
Particle mass flow	2.35×10^{-05}	Kg/s

- Smooth: the blade surfaces are considered to be hydraulically smooth, $k_s = 0$, i.e. without any roughness.
- Rough: in order to represent surface roughness in the CFD computations the roughness is commonly prescribed as an equivalent sand-grain roughness height [45]. In this case, the blade surfaces are computationally roughened uniformly with a roughness level of the equivalent sand-grain roughness (k_s) = 60μm. This particular quantity is selected as a threshold value based on experimental observations such as [12]. The reader is directed towards reference [5] for details of the implementation of wall roughness in CFX.
- Localised roughness: as will be seen later the surface abrasion brought about by SPE acts in a localised manner rather than affecting the entire blade surface. In order to map the regions of SPE action onto patches of roughness an approximate method involving a localised surface perturbation was coded in Matlab. The geometric degree of the surface disturbance is controlled by a "Fraction Factor" parameter that was calibrated by comparison with uniformly roughened cases. This method allows the surface roughness to closely follow the patterns of erosion obtained by the SPE

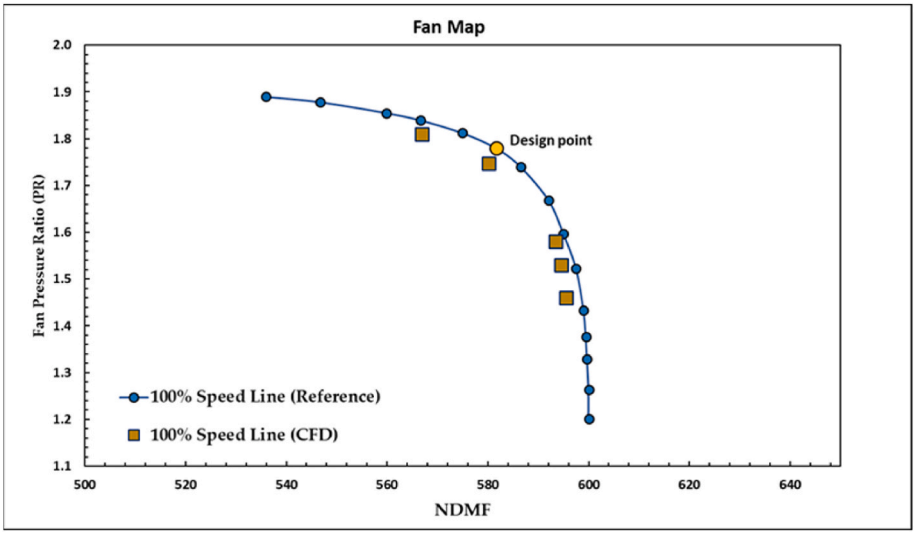


Fig. 4. Comparison between fan design parameters [17] and CFD results, 100% speed-line.

Table 6
Comparison of the numerical results and the design calculation values at design point (DP).

Parameter	CFD results	Reference	Difference (%)
Mass flow ($\dot{m}$) (kg/s)	84.7	83.1	1.8
PR (2-stage booster)	1.3	1.34	2.9
Exit temperature (T_2) at stage 2 exit (K)	344.2	333.0	3.2
Efficiency (2-stages booster)	0.79	0.82	3.6

simulations. Some regions of the blade, such as the near leading-edge region, have a marked impact on the blade aerodynamics to the extent that they dominate the overall production of blockage. This is why one can get comparable results between the local roughness model and the entirely rough 60 μm case once the FF parameter is suitably adjusted.

4. Results and discussion

In compressors, SPE has got two main consequences [40,46]:

- Deformation of the geometry and degradation of the surface quality of the blades.
- Changes to the flow field owing to increasing surface roughness.

In this section, the SPE numerical simulations outcomes are reported. The computations were conducted following the erosion model setup described in Section 3.4. Thus, this section introduces the results of the numerical predictions of SPE effects on the internal components of the LPC. The organisation of this section is as follows. Firstly, the LPC performance results for three cases mentioned above are presented. This is followed by detailed discussions of the particle transport computations, erosion patterns, localised surface roughness evaluation, effect of roughness variation on LPC parameters and velocity distributions. The final element comprises global cycle analysis obtained through the GTE performance code Turbomatch and investigates the link between LPC SPE and cycle performance.

A summary of the computed degradation in the key variables of the LPC against the smooth case is shown in Table 7. The key variables selected to represent the overall performance of the compressor are the pressure ratio (PR), non-dimensional mass flow (NDMF) and the isentropic efficiency (η_{is}) [47]. The results shown in Table 7 indicate the

Table 7
LPC performance parameters for the smooth and two roughness cases.

Case	PR	PR % diff	NDMF	NDMF % diff	η_{is}	η_{is} % diff
Smooth	1.34	–	79.9	–	0.79	–
Rough	1.27	5.2	77.7	2.7	0.72	8.8
Localised roughness	1.26	6.0	76.6	4.1	0.71	10.1

level of performance degradation for the rough and localised roughness cases as percentage deviations from the smooth case. In general, the localised roughness model accentuated the degradation of the performance parameters in comparison with the 60 μm whole blade roughness model the reasons of which will be discussed in a later section.

4.1. Particle transport computations

The air and SPs come into contact with the blades of the LPC at speeds and angles that are functions of the local geometry as well as the rotational velocities of the blade and the particle's shape, velocity and size. A sample of the particle trajectories through the compressor is shown in Fig. 5. In CFX the user has the ability to vary a number of particle tracks for the proposes of postprocessing visualisation. The plot in Fig. 5, portraying the trajectory of the particles coloured by particle velocity and obtained with 85 computed tracks, highlights the general trend of radial migration of the particles between the IGV inlet and S3 discharge stations.

A characterisation of the dynamic interactions of the particles with the surfaces of the blades is done in an illustrative manner in Fig. 6 below employing the LPC IGV and R2 blade components. It is noteworthy the radial migration of the particles due to the combined effect of the rising hub line, which affects the IGV particles, as well as the centrifugal effects brought about the rotation of R2. Particle rebound is apparent in the suction side (SS) of the IGV together with the pressure side (PS) of R2 where a high incidence angle of collision with a surface is evident being brought about by the change of frame of reference of the rotating R2 domain.

4.2. Erosion patterns

The turbomachinery blading erosion which follows the particle impacts presents detectable patterns on the LPC blades surfaces. The heaviest erosion distributions are associated with the outer regions of

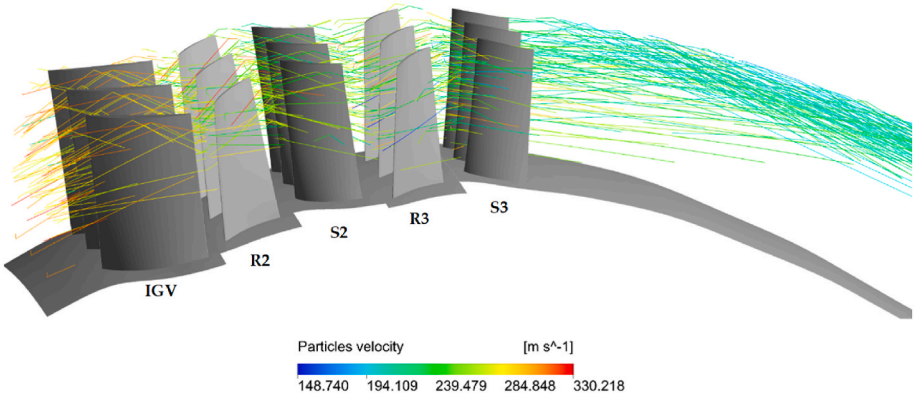


Fig. 5. LPC computed particle trajectories.

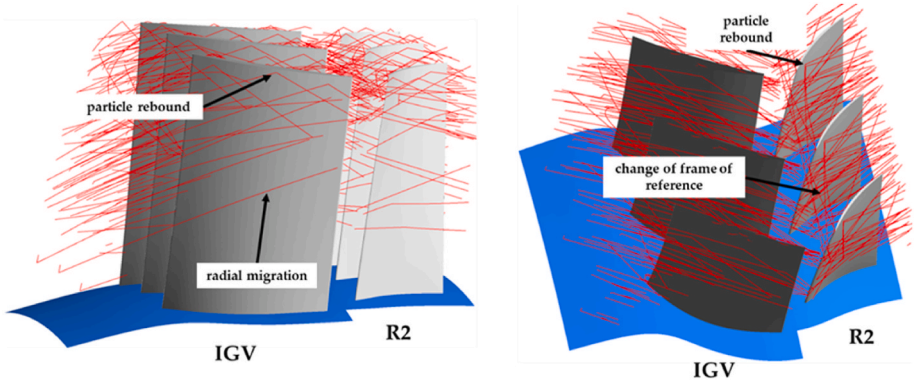


Fig. 6. Sample of particle trajectories for the IGV and R2 blades.

the blades and, in general, tend to affect in different ways the SS and PS of stators and rotors. Fig. 7 presents the distribution of the particle erosion rate density, with units expressed as Kg/s/m^2, over the two sides of the LPC modelled blade rows. In the top section of Fig. 7 it is apparent that the bulk of the eroded regions correspond to the early chord in the SS of the stationary components and the latter part of the chord in the PS of the rotors. As a rule, the most affected regions are the outer sections of the blades. The regions with highest erosion rate densities are depicted in the bottom section of Fig. 7 which presents the distributions of the erosion densities in the PS of the IGV, S2 and S3 as well as the SS of R2 and R3. The erosion patterns portrayed by the bottom section of Fig. 7 present an inversion of the erosion trends identified in the opposite sides of the blades depicted in the upper section of Fig. 7. For the IGV the bulk erosion rate occurs near the trailing edge (TE) and this trend is extensive to S2 and S3 blades. The rotating components, R2 and R3, exhibit high erosion rates in the SS regions of the outer span. These distribution patterns will be associated with localised erosion which requires a flexible representation capable of replicating the spatial variation of surface degradation chordwise and spanwise. The localised surface roughness modelling developed as a part of this research is presented in the following section.

4.3. Localised surface roughness

The erosion rates and the surface roughness have been observed to correlate by considering the variation in the parameters known to affect erosion such as particles density, mechanical properties of the target material, particle velocity, angle of impact and the size of the particles [5]. However, it has also been observed experimentally that the roughness of surfaces exposed to SPE did not tend to increase beyond a given value even though additional mass kept being removed through mechanical abrasion [12]. For axial compressor blades, there is only a limited number of references available in the open literature which present a characterisation of the surface roughness in real world applications [48]. Following Aldi et al. [49], the surface roughness of the compressor blades can be described as follows:

1. The value of $k_s = 5\mu$m denotes a healthy in-service blade.
2. The value of $k_s = 20\mu$m denotes an in-service deteriorated blade which can continue in operation but needs to be monitored.
3. The value $k_s = 40\mu$m denotes an in-service entirely roughened blade surface. At, and above, this level of roughness the key parameters of the engine will be significantly adversely affected. Completely roughened means 100% of the blade area was roughened.

In this study, $k_s = 60\mu$m is specified as limit roughness value beyond which further material removal does not increase surface roughness. According to recent literature, experimental and theoretical efforts are being devoted to characterising the surface roughness of eroded materials [50,51]. However, these studies are not very useful for conducting evaluations of the degradation of turbomachinery components due to the complexity of the flow field involved as well as the intricate nature of the initial interactions of the particles within the machine. In this study, a methodical examination of localised surface roughness was performed on the LPC blades to quantify the effects of roughness on the research engine parameters such as engine pressure ratio (EPR), specific fuel consumption (SFC), temperature entry turbine (TET), etc. This section presents the methodology used in this research to represent localised surface roughness associated with SPE on the LPC blades of the research engine using a surface perturbation technique which is employed to represent the regions of the blades which are affected by erosion. Fig. 8 exemplifies the approach employing one of the profiles used to defined

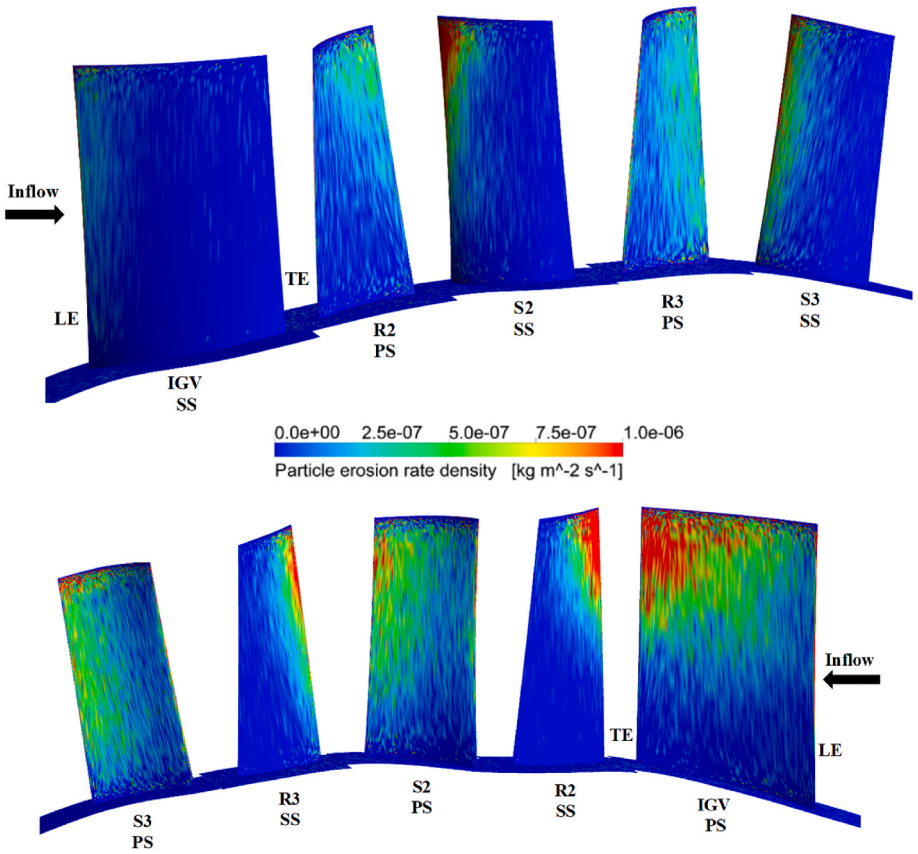


Fig. 7. Erosion patterns of the IGV, R2, S2, R3 and S3 blades, respectively. (Where SS is suction side, PS is pressure side, LE is leading edge and TE is trailing edge.)

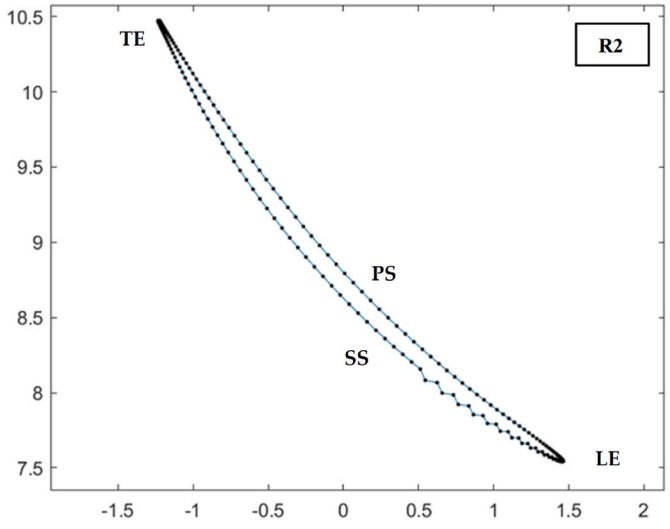


Fig. 8. R2 profile with SS localised roughness geometry perturbation.

the R2 blade geometry. As can be seen in Fig. 8 a section of the SS near the LE of the blade is disrupted to represent local roughness effects.

The severity of the perturbation of the blade geometry is governed in the surface disruption algorithm by a "Fraction Factor" (FF) parameter as demonstrated graphically in Fig. 9. The FF is a geometric perturbation parameter that enables the variation of the severity of the saw tooth crenelations, based on the original airfoil coordinates. The surface roughness induced by the FF parameter is not physical in the sense that it bears no direct relationship to the abrasion patterns brought about by SPE. The approach is however useful in enabling the prescription of selective blade surface roughness patches and lends itself to calibration against the technique used in CFX to impose wall roughness and which consists in the downward shift in the logarithmic velocity profile [31].

Once the location of the roughness patch is determined, based on the qualitative observations of the SPE simulations, the mesh generation of the disrupted surface blade can proceed employing a trial value of the FF parameter, Fig. 10. The analysis of the aerodynamic results permits the adjustment of the FF parameter to represent a local surface roughness corresponding to the 60 μm threshold value.

The placement of the localised roughness patches, Fig. 11, permits a flexible representation of the SPE distributions presented in Fig. 7.

The SPE predictions manifest themselves therefore as an increase in the localised blade surface. roughness together with pitting of the blade surfaces with deep erosion spots/patches. The effects of increasing surface roughness on the aerodynamics and performance of the compressor were then assessed. From our calibration efforts it was observed that an FF parameter equalling 0.5 represents the degradation effects due to SPE induced localised roughness with trends similar to those obtained from the simulations employing entirely roughened blade walls with $k_s = 60\mu$m in terms of the LPC key performance variables.

4.4. *Effects of localised roughness on low-pressure compressor parameters*

The purpose of the localised roughness investigations was to complement the SPE calculations focusing on the more severely eroded regions of the compressor blades. To achieve this goal, a comparison between the smooth, rough and localised roughness simulation results employing the PR, NDMF and isentropic efficiency (η_{is}) parameters was carried out. The computed values correspond to the design point (DP) operating conditions on the 100% speed-line of the research engine. The computed results have been presented above, Table 7.

When the PR, NDMF and η_{is} were determined for the LPC operating

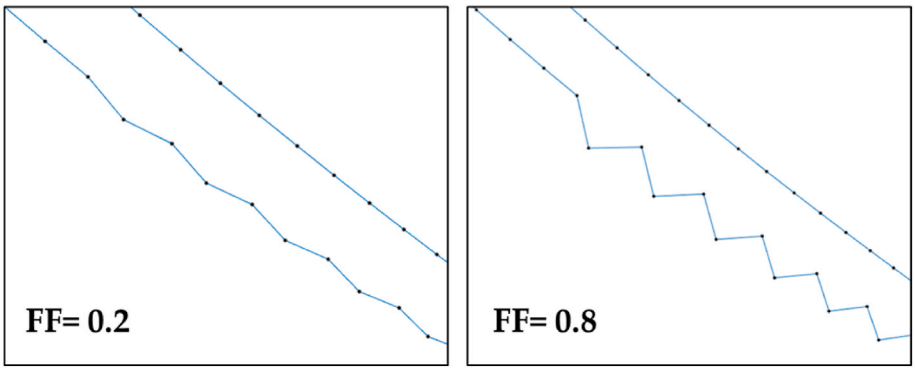


Fig. 9. Localised roughness FF geometry disruption parameter.

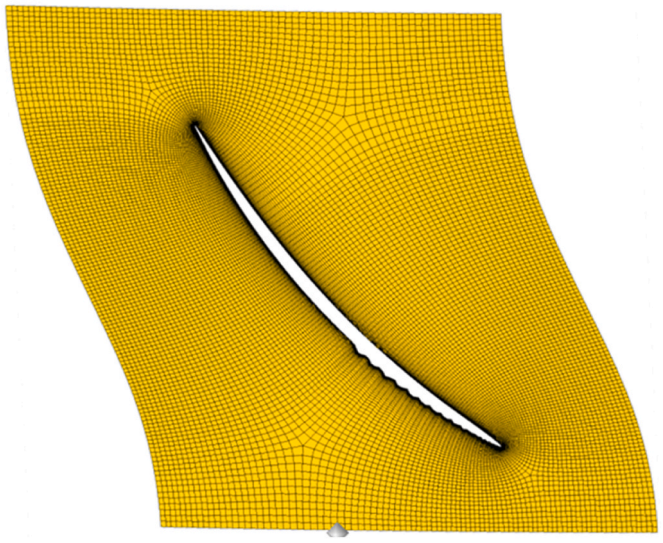


Fig. 10. Localised roughness R2 mesh.

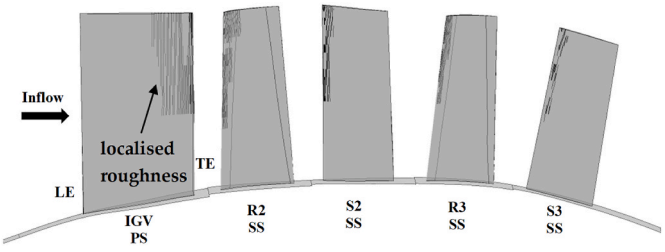


Fig. 11. Positions of localised roughness on the IGV, R2, S2, R3 and S3 blades.

at its DP, it was found that the performance degradation due to the localised roughness exhibited similar trends to those of the 60 μm rough case. For the rough case, it was shown that the deviation of PR, NDMF and η_{is}, by comparison with the hydraulically smooth case, were 5.2, 2.7, and 8.8%, respectively. For the localised roughness case the corresponding deviations were 6.0, 4.1 and 10.1%. The deviation between the computed quantities for the rough and localised roughness cases is 0.8% for PR and 1.3% for the η_{is}. Regarding NDMF the variation is 1.4% which it is indicative of the fact that the blockage effects brought about by the localised roughness procedure described above represents an overestimation of this physical process.

It is readily accepted that the present approach does not seek to replicate in any shape or form the very complex nature of actual surface roughness given its rudimentary nature. Further, it has limitations as a quantitative methodology to represent the SPE aerodynamic impact on the LPC performance. However, it provides the means to account for the link between the erosive phenomenon and the aerodynamic degradation of the compressor within an acceptable band of agreement (<1.4%) whilst taking into account the distributed nature of the SPE interaction with the blades.

4.5. *Blade-to-blade flow details*

Blade-to-blade flow distributions corresponding to the smooth, rough, and localised roughness cases are presented in this section. The simulated axial velocity contours at 85% of the span are shown in Fig. 12. The results describe the flow field in the IGV and the first stage of the LPC comprising the R2 and S2 passages. The comparison between the hydraulicly smooth and the rough ($k_s = 60\mu$m) cases reveals an essentially similar flow structure which is characterised by small regions of flow separation near the TE of each blade row. These regions of low flow momentum show an increase in area for the localised roughness case when compared with the entirely roughened case. It is noteworthy to observe that the roughened sections of R2 and S2 blade rows, corresponding to the first 20% of the chord, are associated with a thickening of the boundary layers leading to an earlier separation under the diffusive conditions that apply on the latter section, chordwise, of the

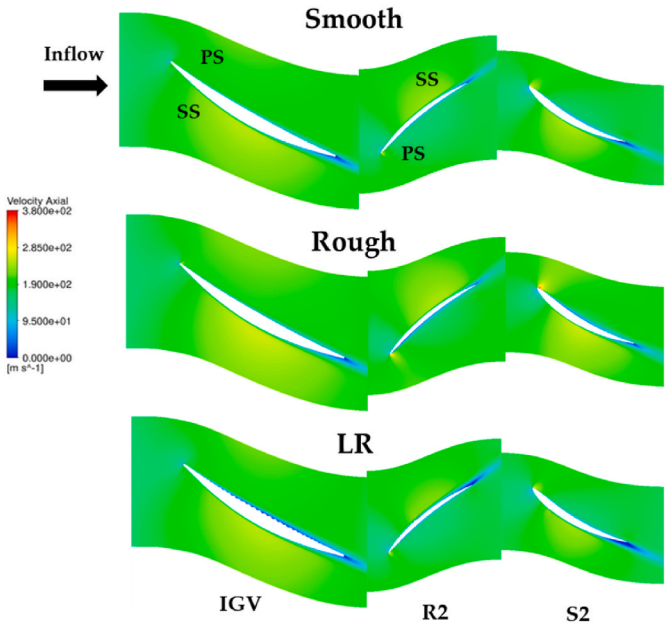


Fig. 12. Axial velocity contours for IGV, R2 and S2, 85% span, for Smooth, Rough and Localised Roughness (LR) cases.

compressor blades leading thereby to an expansion of the separation regions. These are in turn responsible for the added blockage which is manifested as a decrease in the NDMF parameter noted above.

4.6. Wakes characterisation

The three roughness conditions mentioned above are examined next from the perspective of the distributions of axial velocity downstream of the first three components of the LPC, IGV, R2 and S2. Fig. 13 presents pitch-wise distributions of axial velocity at mid span of these three blade rows. The velocity defect associated with IGV is of the order of 120 m/s for the hydraulically smooth blade condition and these values are exceeded for the $k_s = 60\mu$m case as well as the localised roughness model. The localised roughness is applied on this blade on the PS and this associated with a local thickening of the boundary layer. For R2 and S2 the provision of additional roughness, of either description, lead to a substantial increase of the velocity defect downstream of the blade which is indicative of intensification of the diffusive process brought about by the roughening of the blade surfaces. This in turn equates to a thickening of the SS boundary layers as is evident in the R2 and S2 plots of Fig. 13.

A characterisation of the span wise flow field in the wake regions is performed by reference to the flow downstream of the R3 component, Fig. 14, for the three roughness cases studied. The flow in these transversal planes exhibits four regions whose flow structures are worthy of further discussion, namely the low momentum near shroud tip leakage region, the blade wake, the hub corner stall and the radial distribution of axial velocity whose peak is located at around 25% of the span. On the whole tip leakage region has got a similar distribution across the three cases studied. Its origin is associated with the over blade jet brought about by the difference in pressure between the PS and the SS. Regarding the wakes it is apparent that the introduction of roughness broadens the wake especially in the upper regions of the span. Near the hub a corner stall is apparent for all cases but the comparison of the plots leads to the interesting observation that the introduction of roughness tends to suppress, though not entirely eliminate, the intensity and extent of the corner stall. Although the span-wise distribution of the three-dimensional velocity is essentially uniform, the contribution of the axial velocity varies sharply with the span and has an intense peak at about 25% of the span.

4.7. Turbomatch performance tool

The thermodynamic cycle performance computations were performed using the Turbomatch 0-D engine performance in-house code. In Turbomatch scaled maps are used to represent the compressor, combustor and turbine. These are combined with modules which describe the various subcomponents of the GTE, known as bricks. An explanation of the working criteria and operation principles of the Turbomatch software are found in references [40, 52–54].

Turbomatch is used in the present study to investigate the E3 [17–19] engine inspired model used to study the degradation effects brought about by SPE induced blade surface roughness. Key engine performance parameters, PR, NDMF and efficiency were varied to match

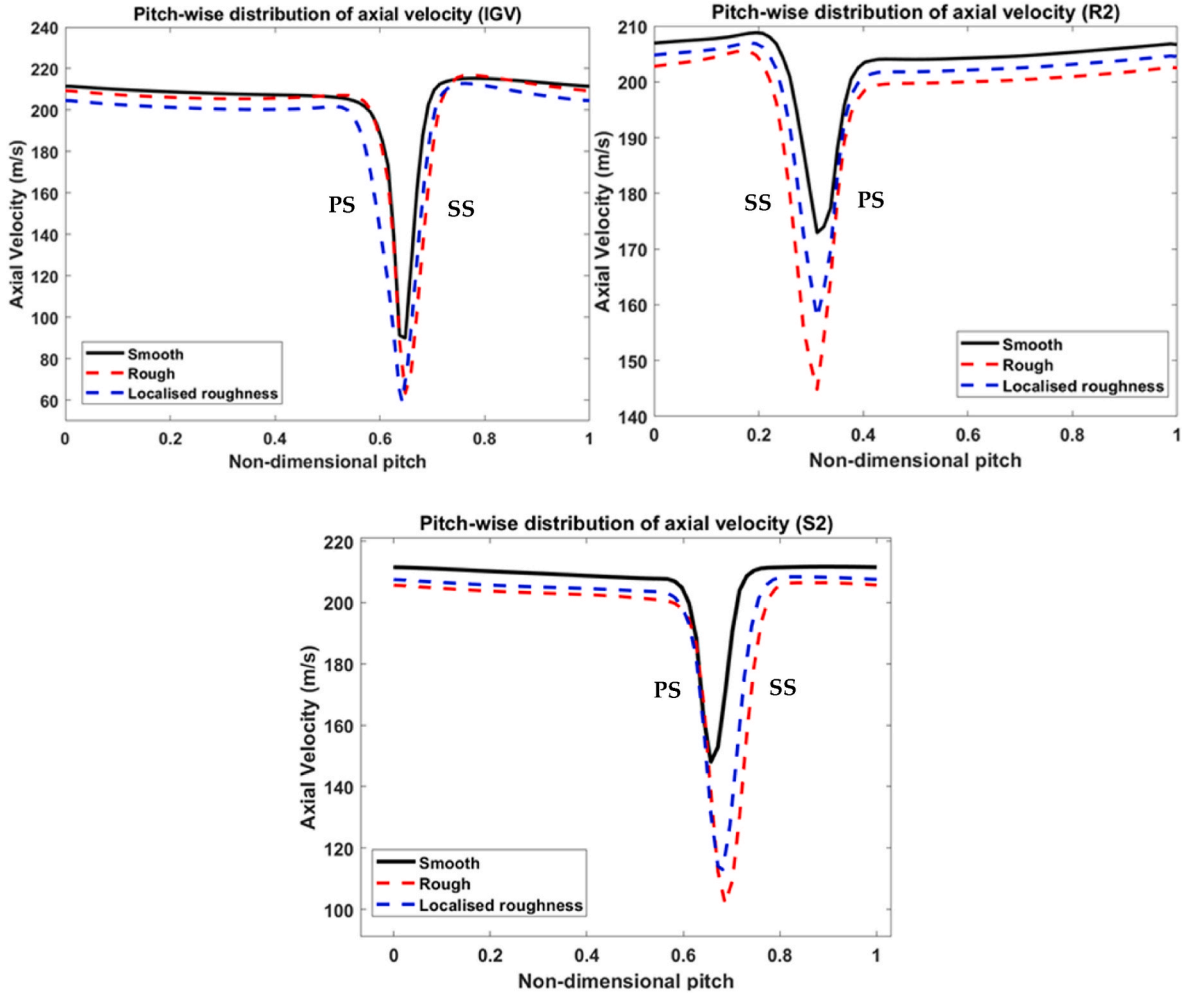


Fig. 13. Distribution of axial velocity as a function of non-dimensional pitch for the IGV, R2 and S2 at 50% span.

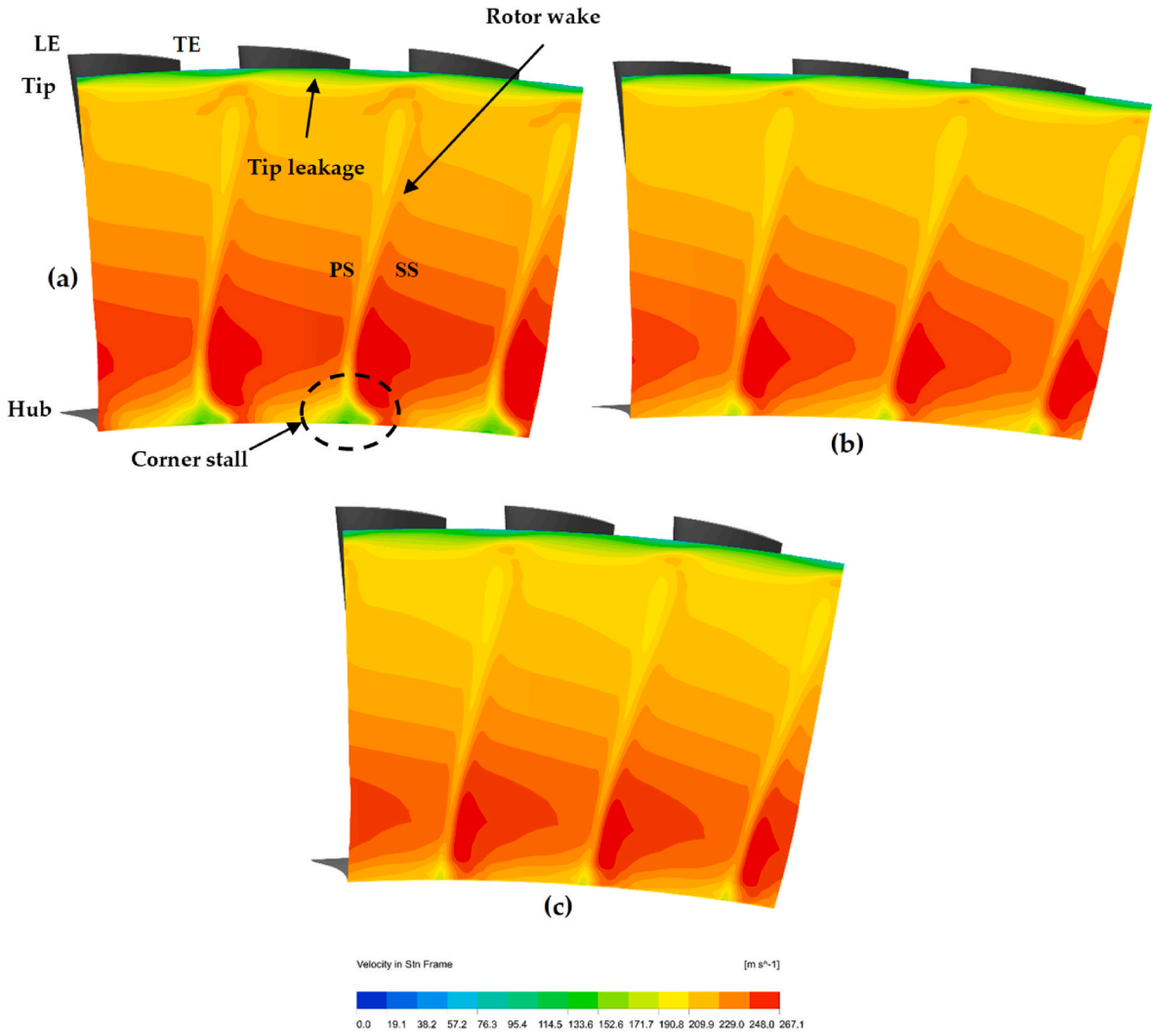


Fig. 14. Distribution of velocity in stationary frame of reference at exit of R3 for (a) Smooth, (b) Rough, and (c) Localised Roughness.

the degradation levels listed in Table 7 and these were used to computed the degradation values of Table 8 using the Turbomatch software.

The specific fuel consumption (SFC), turbine entry temperature (TET), and Engine pressure ratio (EPR) for the entire cycle were calculated. The power setting is governed by a "handle" which is a variable that will determine the matching conditions of the engine. For this set of calculations TET was selected as the handle with the variation of this quantity being due to the changes of the parameters which describe the various degradation states as listed in Table 8. A schematic representation of the research engine is shown in Fig. 15 identifying the separate modules which are known as "bricks" in Turbomatch: Intake, Fan, Bypass duct/flow splitter for bleed (Premas brick), LPC, area of mixing of two flows (Mixess brick), afterburner/intercooler duct (Ducter brick), Bypass nozzle, high-pressure compressor (HPC), Burner, high-pressure turbine (HPT), low-pressure turbine (LPT), and core nozzle. The bricks are linked together, with interfaces known as stations [40].

Table 8
Reduction in PR, NDMF, and η_{is} of the first two booster stages relative to the smooth case.

Case	Reduction		
	PR	NDMF	η_{is}
Smooth	–	–	–
Rough	0.982	0.972	0.940
Localised roughness	0.974	0.961	0.931

4.7.1. *Turbomatch model verification*

A comparison of the Turbomatch findings against the E3 design data [17–19] is reported next for the 100% speed-line. The design point comparison employs the values of temperature at discreet stations of the E3 GTE corresponding stations of the Turbomatch model, Fig. 16.

As can be seen in Fig. 16 the agreement between the computed values and design data is very good throughout with the deviations not exceeding 4%. The missing points correspond to instances for which no E3 data is available although the Turbomatch model required provision of these components.

4.8. *Turbomatch performance results*

This section reports the results of a thermodynamic study performed with the Turbomatch software to investigate the performance of the LPC for the smooth, rough and the localised roughness cases. In order to examine the performance deterioration of the two stages of the LPC, the booster compressor of the research engine was split into two parts. The stages simulated in CFD together with the latter two stages of the LPC were scaled in Turbomatch as two separate components. In order to represent the performance degradation of turbomachinery components in Turbomatch the user specifies a reduction in PR, NDMF and the isentropic efficiency as handle parameters. The relevant values were

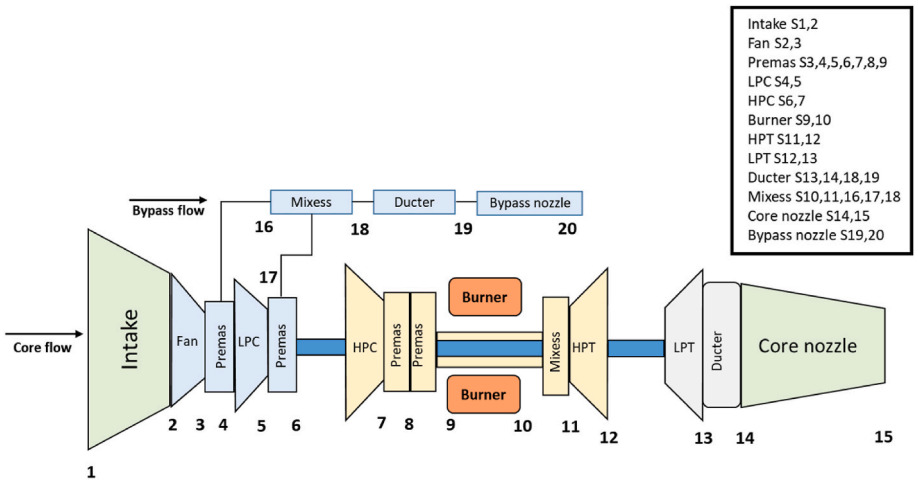


Fig. 15. Turbomatch model of the research engine with station numbering.

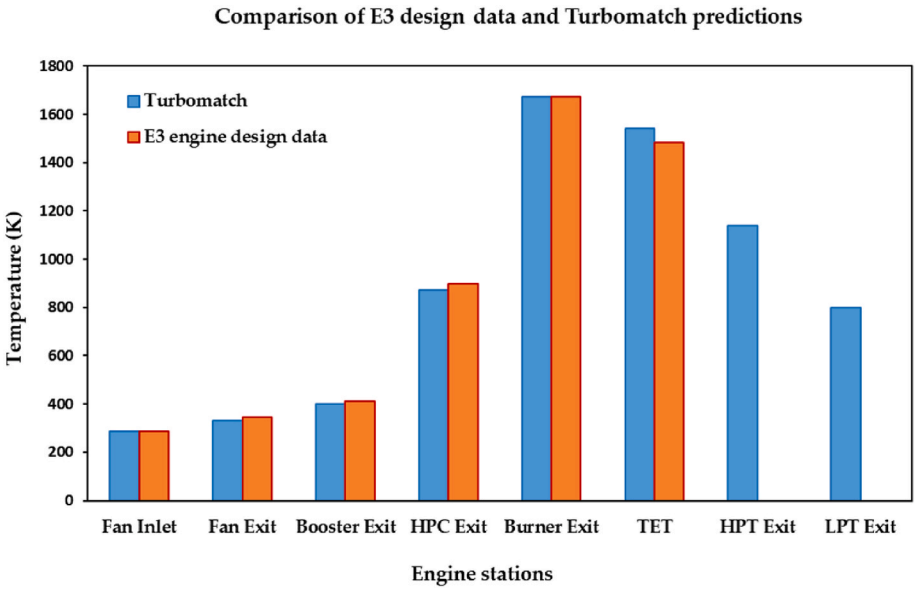


Fig. 16. Turbomatch results against the theoretical design data of E3 engine.

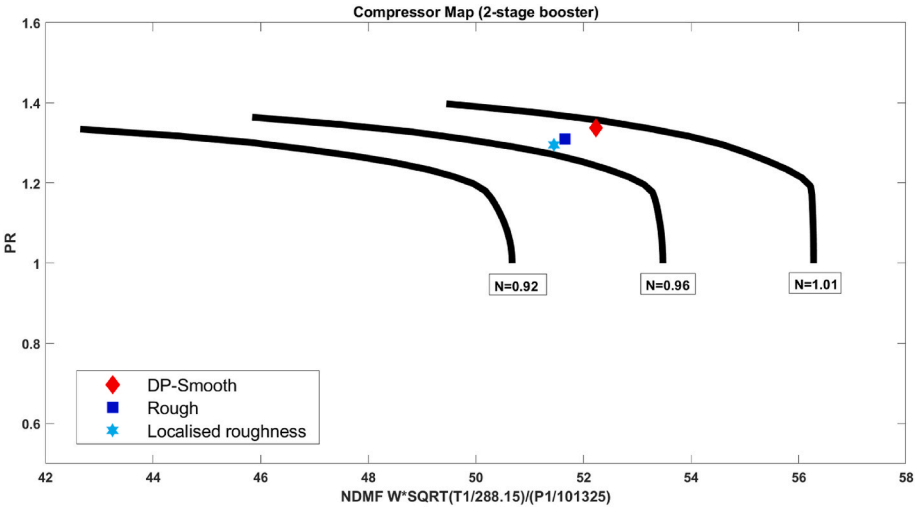


Fig. 17. Compressor map of the 2-stage booster (PR).

obtained from the earlier CFD analyses. The handle input data which characterise the effect of the roughness on the LPC and engine performance variables are shown in Table 8. The outcomes of the Turbomatch model represent:

- The impacts of the roughness conditions on the compressor maps.
- The degradation of the GTE variables in terms of the engine pressure ratio (EPR), specific fuel consumption (SFC) and turbine entry temperature (TET).

4.8.1. *Effect on compressor maps and cycle parameters*

The performance implications of the roughened conditions on the LPC maps were examined by applying the variables degradation values identified in Table 8.

An investigation of the effects of the roughened stages was performed at the DP. The deviation in the characteristic maps of the first two stages of the LPC is presented in Figs. 17 and 18 as PR and isentropic efficiency against the NDMF, respectively. The lines denoted in black in these plots represent the three rotational speeds (N) utilised in the performance analyses. The values of PR and isentropic efficiency for the DP were obtained at 100% N for the smooth case. As the roughness on the blades surface increased, the DP shifts away from its original location and the compressor operating point moves towards a lower mass flow, lower PR and lower isentropic efficiency as seen in Figs. 17 and 18, respectively.

The compressor maps are presented in terms of PR and isentropic efficiency for three speed-lines, N = 0.92, 0.96 and 1.01. The corresponding values for each of these quantities at design point for the smooth, rough and the localised roughness model are depicted as coloured points in the maps. The effect of the introduction of roughness impacts the PR as a reduction in PR value and a shift towards a lower NDMF value as can be seen in the plot presented in Fig. 17. This decrease applies to both roughness cases studied but the difference between the $k_s = 60\mu$m case and the distributed roughness case is smaller than that of the rough case versus hydraulically smooth blading case. Regarding isentropic efficiency the trend observed for PR is repeated with this quantity, Fig. 18.

SPE leads to increased surface roughness of the compressor blades and this will be reflected in a variation in the values of EPR, SFC and TET of the research engine. Table 9 presents the Turbomatch results for the research engine. As can be seen the decrease in EPR between the smooth and rough case is relatively minor (0.63%) but the specification of localised roughness represents an increase of around 60.1% by comparison with the $k_s = 60\mu$m case. Regarding the SFC the inclusion of roughness leads to an increase of this parameter with a difference between the two roughened cases corresponding to a rise of 68%. The final parameter presented in Table 9 demonstrates that the penalty of the operation with roughened turbomachinery components has implications which affect the durability of the GTE through a rise in the TET which will impact in the long term the life of the turbine. The HPT is very sensitive to any increases in inlet temperature because this is linked with creep life reduction and consequently with durability and maintenance requirements of the engine, in addition to any mismatch that might occur between the components of the GTE.

To better understand the implications of the roughened surfaces on both the whole engine and LPC performance, a combination of CFD and Turbomatch investigations were performed. The results are shown in Table 10, where the column headed CFD refers to the LPC and the column headed Turbomatch refers to the overall performance of the research engine. It can be observed that a significant degradation of the LPC performance is forecasted by the CFD simulations, but this impacts in a less significant manner on the overall cycle performance parameters, SFC, TET and EPR. To demonstrate the effects of the increasing the SPE generated surface roughness, Table 10 presented a comparison of the differences of the outcomes between the rough and localised roughness and the smooth case.

The values listed in Table 10 show a significative decrease in the performance parameters of the LPC and the research engine in

Table 9
Effect of the roughness cases on performance variables of the research engine.

Case	Differences with Smooth case (%)		(Δ)
	EPR	SFC	TET (K)
Smooth	–	–	–
Rough	−0.63	+0.50	+13.7
Localised roughness	−1.03	+0.73	+21.1

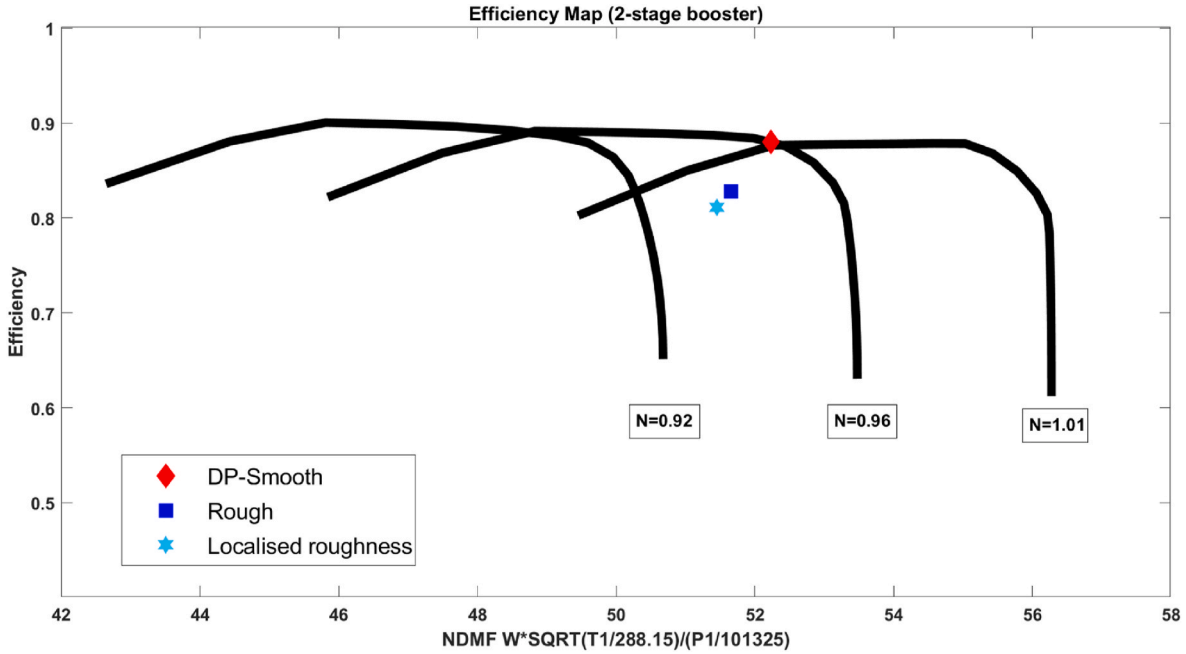


Fig. 18. Compressor map of the 2-stage booster (isentropic efficiency).

Table 10
Comparison of the outcomes between rough and localised roughness of the research engine.

Case	Differences from Smooth case (%)					
	CFD			Turbomatch		
	PR	NDMF	η_{is}	EPR	TET	SFC
Rough	−5.2	−2.7	−8.8	−0.63	+0.82	+0.50
Localised roughness	−5.9	−4.1	−10.1	−1.03	+1.25	+0.73

comparison to the smooth case. This reduction in performance applies especially to the low-pressure compression system which is the GTE component more directly exposed to the erosive action brought about by operation under SPE conditions. The numerical predictions due to the CFD simulations identified a substantial decrease in PR, NDMF and isentropic efficiency. It is interesting to observe that the localised roughness models predict losses that exceed those of the $k_s = 60\mu$m rough case despite the fact that the roughened regions occupy a fraction of the blade surface by comparison with the entirely roughened blades used in the rough case. This observation reinforces the notion that the SPE action affects critical areas of the blading chordwise and hence triggers a rise in the losses which is disproportionate to the extent of the roughness affected region. The implications over the thermodynamic cycle are less severe however as can be seen in Table 10.

5. Conclusion

In this study, numerical predictions of SPE applied to the first two stages of the booster compressor of a research engine based on NASA's E3 GTE are reported together with the thermodynamic cycle implications due to the introduction of SPE induced roughness. The tools employed in the study include the commercial CFD code ANSYS CFX 19.1 and the Cranfield University in-house performance code Turbomatch. The regions of the blades exposed to abrasion through the SPE action are deemed to attain a fully roughened limit surface condition such as was identified experimentally by Hamed et al. [12]. In order to represent the spatial distribution of roughness which correlates with SPE effects, a Matlab script was developed to enable the selective disruption of the blade defining airfoils. The magnitude of the surface perturbation was calibrated against the $k_s = 60\mu$m roughness threshold. The key conclusions which can be drawn from the present study are listed as follows:

- The numerical calculations for the fan map present a good match with the research engine design data with the PR and NDMF predictions discrepancies being 2.8 and 1.9%, respectively.
- Regarding the booster simulations the differences in mass flow, PR (two stages), stage two exit temperature and isentropic efficiency are, 1.8, 2.9, 3.2 and 3.6%, respectively.
- It has been demonstrated that it is possible to selectively roughen discreet regions of the blades to replicate the spatial distributions predicted by the SPE numerical computations.
- The introduction of roughness applied to the entire blade surfaces with $k_s = 60\mu$m entails a 5.2% PR decrease, 2.7% NDMF reduction and a drop of 8.8% in isentropic efficiency. The corresponding drops for the SPE related localised roughness model are 6.0, 4.1 and 10.1%.
- The SPE simulations were carried out with the Tabakoff and Grant erosion model and employed quartz-aluminium material version. 200,000 particles were employed with a minimum dimeter of 20 μm and a maximum dimeter of 80 μm. For the cases examined the peak erosive action takes place in the PS of the IGV and SS of R2 and R3. In general, the rotor PS is affected towards the latter section of the chord whilst on the SS of the rotors the peak erosion occurs near the LE.
- The presence of SPE induced roughness is translated by a deepening of the velocity defects in the wakes and the thickening of the SS boundary layer. There is evidence that the presence of roughness contributes to a reduction of the hub corner stall by reference to the smooth case.
- The thermodynamic implications of the SPE erosive action have been investigated through Turbomatch simulations. The decrease in PR, NDMF and isentropic efficiency of the first two booster stages relative to the smooth case are 0.982, 0.972 and 0.940, respectively for the $k_s = 60\mu$m rough case. The corresponding localised roughness values are 0.974, 0.961 and 0.931.
- Regarding the cycle degradation consequences there is a decrease of 0.63 and 1.03% respectively for the rough and the localised roughness cases in terms of EPR. The TET parameter however increases from 0.82% to 1.25% for these two cases. This finding indicates that the occurrence of SPE has an attendant implication for the durability of the GTE. There is an addition an economic and environmental penalty which is expressed as a 0.50% SFC increase for the uniformly roughened case and 0.73% for localised roughness situation.

It is a fact that the SPE action has a very marked and uneven spatial distribution and that is the reason we sought a methodology to primarily qualitatively replicate it, whilst providing a measure via the calibration, of quantitative performance assessment. This patchy distribution cannot be adequately represented through a uniform added roughness. The results returned by the localised roughness approach are comparable, though not equal, to the results obtained from the 60 μm entirely roughened blade. We sought primarily to present an expedient methodology that reflects the uneven distribution mentioned above. For the purposes of this paper that methodology is reliant on the calibration exercise although neither approach (localised vs whole blade) offers a particularly accurate description of an SPE roughened blade. Whether the localised roughness technique remains so will require further investigations.

Credit author statement

Jasem Alqallaf: Conceptualization, Methodology, Resources, Software, Validation, Visualisation, Writing- Original draft preparation. **Joao Amaral Teixeira**: Data curation, Supervision, Visualisation, Writing- Reviewing and Editing.

Funding

This research received no external funding.

Declaration of competing interest

The authors declare that they have no known competing financial interests or personal relationships that could have appeared to influence the work reported in this paper.

Acknowledgments

The authors of this article are grateful and acknowledge the help provided by their institutes. Also, a thank you to Dr Natan Zawadzki for his E3 inspired research engine model.

References

[1] A. Vogel, A. Durant, M. Cassiani, R. Clarkson, M. Slaby, S. Diplas, K. Kruger, A. Stohl, Simulation of volcanic ash ingestion into a large aero engine: particle–fan interactions, J. Turbomach. 141 (1) (Jan. 2019) 1–12.
[2] W. Tabakoff, Compressor erosion and performance deterioration, J. Fluid Eng. 109 (3) (Sep. 1987) 297–306.

[3] K. Brun, M. Nored, R. Kurz, Analysis of solid particle surface impact behavior in turbomachines to assess blade erosion and fouling, Proc. 41 Turbomach. Symp. (2012) 1–17.
[4] P. Venturini, M. Andreoli, D. Borello, F. Rispoli, S. Gabriele, Modeling of water droplets erosion on a Subsonic compressor cascade, Flow, Turbul. Combust. 103 (4) (2019) 1109, 1125, Nov.
[5] J. Alqallaf, N. Ali, J.A. Teixeira, A. Addali, Solid particle erosion behaviour and protective coatings for gas turbine compressor blades—a review, Processes 8 (8) (Aug. 2020) 1–33.
[6] X. Bai, Y. Yao, Z. Han, J. Zhang, S. Zhang, Study of solid particle erosion on helicopter rotor blades surfaces, Appl. Sci. 10 (3) (Feb. 2020) 977.
[7] A. Evstifeev, N. Kazarinov, Y. Petrov, L. Witek, A. Bednarz, Experimental and theoretical analysis of solid particle erosion of a steel compressor blade based on incubation time concept, Eng. Fail. Anal. 87 (May 2018) 15–21.
[8] R. Kurz, K. Brun, Degradation in gas turbine systems, J. Eng. Gas Turbines Power 123 (1) (Jan. 2001) 70–77.
[9] F. Melino, M. Morini, A. Peretto, M. Pinelli, P. Ruggero Spina, Compressor fouling modeling: relationship between computational roughness and gas turbine operation time, J. Eng. Gas Turbines Power 134 (5) (May 2012) 1–8.
[10] E. Bousser, L. Martinu, J.E. Klemberg-Sapieha, Solid particle erosion mechanisms of hard protective coatings, Surf. Coating. Technol. 235 (Nov. 2013) 383–393.
[11] W. Tabakoff, A. Hamed, V. Shanov, Blade deterioration in a gas turbine engine, Int. J. Rotating Mach. 4 (4) (1998) 233–241.
[12] A. Hamed, W.C. Tabakoff, R.V. Wenglarz, Erosion and deposition in turbomachinery, J. Propul. Power 22 (2) (Mar. 2006) 350–360.
[13] A. Ghenaiet, Study of sand particle trajectories and erosion into the first compression stage of a turbofan, J. Turbomach. 134 (5) (Sep. 2012) 1–17.
[14] M. Suzuki, M. Yamamoto, Numerical Simulation of Particulate Erosion in Two-Stage Compressor 1 (1) (2014) 2742–2753.
[15] E. Poursaeidi, H. Tafrishi, H. Amani, Experimental-numerical investigation for predicting erosion in the first stage of an axial compressor, Powder Technol. 306 (Jan. 2017) 80–87.
[16] W. Tabakoff, Study of single-stage axial flow compressor performance deterioration, Wear 119 (1) (Sep. 1987) 51–61.
[17] J.E. Halle, C.J. Michael, Energy Efficient Engine fan component detailed design report, U.S. Dep. Energy Off. Sci. Tech. Inf. (6467188) (Sep. 1981) 1–127. CR-165466.
[18] C.J. Michael, J.E. Halle, Energy efficient engine low-pressure compressor component test hardware detailed design report, U.S. Dep. Energy Off. Sci. Tech. Inf. (1983002215) (1981) 1–98. CR-165354.
[19] D.E. Gray, Energy efficient engine preliminary desighn and integration studies report, U.S. Dep. Energy Off. Sci. Tech. Inf. (1979000391) (1978) 1–366. CR-135396.
[20] A. El-Sayed, Taylor & Francis Group, in: second ed.Aircraft propulsion and gas turbine engines, 5, 2017, 1, London.
[21] M. Parsi, K. Najmi, F. Najafifard, S. Hassani, B.S. McLaury, S.A. Shirazi, A comprehensive review of solid particle erosion modeling for oil and gas wells and pipelines applications, J. Nat. Gas Sci. Eng. 21 (Nov. 2014) 850–873.
[22] H. Arabnejad, A. Mansouri, S.A. Shirazi, B.S. McLaury, Development of mechanistic erosion equation for solid particles, Wear 332 (333) (May 2015) 1044–1050.
[23] ANSYS, ANSYS CFX-Solver Modeling Guide, 2018. Canonsburg, PA.
[24] A. Ghenaiet, Modeling of particle trajectory and erosion of large rotor blades, Int. J. Aerosp. Eng. (2016) 1–15, 2016.
[25] B.E. Lee, J.Y. Tu, C.A.J. Fletcher, On numerical modeling of particle–wall impaction in relation to erosion prediction: Eulerian versus Lagrangian method, Wear 252 (3–4) (Feb. 2002) 179–188.
[26] A. Sokolichin, G. Eigenberger, A. Lapin, A. Lübert, Dynamic numerical simulation of gas-liquid two-phase flows Euler/Euler versus Euler/Lagrange, Chem. Eng. Sci. 52 (4) (Feb. 1997) 611–626.
[27] F. Greifzu, C. Kratzsch, T. Forgber, F. Lindner, R. Schwarze, Assessment of particle-tracking models for dispersed particle-laden flows implemented in OpenFOAM and ANSYS FLUENT, Eng. Appl. Comput. Fluid Mech. 10 (1) (Jan. 2016) 30–43.
[28] F.-K. Benra, H.J. Dohmen, J. Pei, S. Schuster, B. Wan, A Comparison of one-way and two-way coupling methods for numerical analysis of fluid-structure interactions, J. Appl. Math. 2011 (2011) 1–16.
[29] A. Ghenaiet, S.C. Tan, R.L. Elder, Prediction of an axial turbomachine performance degradation due to sand ingestion, Proc. Inst. Mech. Eng. Part A J. Power Energy 219 (4) (Jun. 2005) 273–287.
[30] A. Haider, O. Levenspiel, Drag coefficient and terminal velocity of spherical and nonspherical particles, Powder Technol. 58 (4) (Apr. 1988) 63–70.
[31] ANSYS, ANSYS CFX-Solver Theory Guide, 2016. Canonsburg, PA.
[32] R. Mei, An approximate expression for the shear lift force on a spherical particle at finite Reynolds number, Int. J. Multiphas. Flow 18 (1) (Jan. 1992) 145–147.
[33] I. Finnie, Some reflections on the past and future of erosion, Wear 186–187 (Jul. 1995) 1–10.
[34] S. Qian, S. Kanamaru, Verification of CFD prediction accuracy of particle and droplet induced erosion rate for engineering applications, MATEC Web of Conferences 333 (2021) 1–6.
[35] I. Finnie, Erosion of surfaces by solid particles, Wear 3 (1960) 87–103.
[36] G. Grant, W. Tabakoff, An experimental investigation of the erosive characteristics of 2024 aluminum alloy, Natl. Tech. Inf. Serv. U. S. Dep. Commer. (1) (1973) 1–49. DA-ARO-D-1.
[37] M.-W. Kang, N. Park, S.-H. Suh, Numerical study on sediment erosion of francis turbine with different operating conditions and sediment inflow rates, Procedia Eng. 157 (2016) 457–464.
[38] G. Enikeev, A. Abdulin, R. Yanibaev, A. Kasatkin, Analysis of the particle motion dynamics in the compressor to accompany erosion resistance testing of blade material, 2020 Int. Conf. Dyn. Vibroacoustics Mach. (DVM). IEEE (Sep. 2020) 1–8.
[39] B.N. Bhat, B. Pandey, A.S. Tamirisakandala, M.V. Nathal, Aerospace materials characteristics, Am. Inst. Aeronaut. Astronaut. M17–6171 (2018) 1–145.
[40] J. Alqallaf, J.A. Teixeira, Blade roughness effects on compressor and engine performance—a CFD and thermodynamic study, Aerospace 8 (330) (Nov. 2021) 1–29.
[41] Lucideon, Silica - silicon dioxide (SiO2), Lucideon Mater. Dev. Commer. 1 (2001) 1–6. Stoke-on-Trent.
[42] N. Bojdo, A. Filippone, A Simple model to assess the role of dust composition and size on deposition in rotorcraft engines, Aerospace 6 (44) (Apr. 2019) 1–26.
[43] V.B. Nguyen, Q.B. Nguyen, Y.W. Zhang, C.Y.H. Lim, B.C. Khoo, Effect of particle size on erosion characteristics, Wear 348 (349) (Feb. 2016) 126–137.
[44] R. Loud, A. Slaterpryce, Gas Turbine Inlet Air Treatment, GE Power Gener., 1991, pp. 1–26. GER-3419A.
[45] A. Zamiri, S.J. You, J.T. Chung, Surface roughness effects on film-cooling effectiveness in a fan-shaped cooling hole, Aero. Sci. Technol. 119 (107082) (Dec. 2021) 1–17.
[46] B. Mohammadi, A. Khoddami, Representative volume element-based simulation of multiple solid particles erosion of a compressor blade considering temperature effect, Proc. Inst. Mech. Eng. Part J J. Eng. Tribol. 234 (8) (2020) 1173, 1184, Aug.
[47] R. Kurz, C. Meher-Homji, B. Fellow, K. Brun, J. Moore, Gas turbine performance and maintenance, in: Proceedings of the 41st Turbomachinery Symposium, 2013, pp. 1–32. Houston, TX.
[48] E. Syverud, L.E. Bakken, The impact of surface roughness on axial compressor performance deterioration, in: ASME Turbo Expo 2006: Power for Land, Sea and Air, 2006, pp. 1–11. Barcelona.
[49] N. Aldi, M. Morini, M. Pinelli, P.R. Spina, A. Suman, M. Venturini, Performance evaluation of nonuniformly fouled Axial compressor stages by means of computational fluid dynamics analyses, J. Turbomach. 136 (2) (Feb. 2014) 1–11.
[50] Z. Li, Y. Liu, Optimization of rough transonic axial compressor, Aero. Sci. Technol. 78 (Jul. 2018) 12–25.
[51] H. Seehausen, P. Gilge, A. Kellersmann, J. Friedrichs, F. Herbst, Numerical study of stage roughness variations in a high pressure compressor, Int. J. Gas Turbine, Propuls. Power Syst. 11 (3) (2020) 1–10.
[52] L. Gallar, V. Volpe, M. Salussolia, V. Pachidis, A. Jackson, Thermodynamic gas model effect on gas turbine performance simulations, J. Propul. Power 28 (4) (Jul. 2012) 719–727.
[53] S. Sampath, T. Nikolaidis, P. Pilidis, 'Turbomatch-webengine' – a web based gas turbine engine performance analysis tool, *Awatef Hamed, Fac. Work Res. Coll. Eng. Appl. Sci.*, no. ISABE-2015-20125 (Nov. 2015) 1–8.
[54] A. Nind, V. Sethi, S. Sampath, "Towards the development of A Technoeconomic, environmental risk analysis for an aircraft operator, Awatef Hamed, Fac. Work Res. Coll. Eng. Appl. Sci (2015) 1–10. ISABE-2015-20214.



https://dspace.org/

Numerical study of effects of solid particle erosion on compressor and engine performance

Alqallaf, Jasem; Teixeira, Joao Amaral

2022-06-24
Elsevier
https://doi.org/10.1016/j.rineng.2022.100462
Alqallaf J, Teixeira JA. (2022) Numerical study of effects of solid particle erosion on compressor and engine performance. Results in Engineering, Volume 15, September 2022, Article number 100462

Downloaded from a DSpace repository. https://dspace.org/